In situ characterisation of dynamic fracture in Al_2O_3 using ultra-fast X-ray phase contrast radioscopy: effects of porosity and crack speed

Quentin Henry, Jean-Benoit Kopp, Louise Le Barbenchon, Jérémie Girardot, Bratislav Lukic, Amitay Cohen, Antonio Cosculluela, Philippe Viot

Int J Fract
https://doi.org/10.1007/s10704-024-00816-0

RESEARCH

In situ characterisation of dynamic fracture in Al_2O_3 using ultra-fast X-ray phase contrast radioscopy: effects of porosity and crack speed

Q. Henry · J.-B. Kopp · L. Le Barbenchon · J. Girardot · B. Lukić · A. Cohen · A. Cosculluela · P. Viot

Received: 5 June 2024 / Accepted: 11 December 2024

Abstract The dynamic fracture properties of porous ceramics were studied using single bunch synchrotron X-ray phase contrast imaging. The modified brazilian geometry was used to initiate and propagate a pure mode I crack. The specimen was compressed using the Split Hopkinson bars at strain rates of the order of 10^2 s^{-1}. Main cracks were isolated for four different grades of Al_2O_3, one dense alumina, and three porous grades with 20 % to 60 % porosity. The maximum measured crack velocities for three grades is of the order of $0.6c_R$ and $0.4c_R$ for the most porous. The fracture energy was estimated using a FE numerical simulation to quantify the influence of inertial effects induced by crack propagation. The results show that these inertial effects are far from negligible (up to 80 % of the stored energy) and that the dynamic correction factors known from the literature tend to overestimate the fracture energy. The values obtained vary from 22 J/m^2 for the densest to 5 J/m^2 for the most porous.

Keywords Porous alumina · Microstructural characterisation · Fracture properties · Dynamic Brazilian test · Ultra-fast X-ray radiography · ESRF

Q. Henry · J.-B. Kopp (✉) · L. Le Barbenchon · J. Girardot · P. Viot
Arts et Metiers Institute of Technology, University of Bordeaux, CNRS, Bordeaux INP, Hesam Universite, I2M, UMR 5295, 33400 Talence, France
e-mail: jean-benoit.kopp@ensam.eu

B. Lukić
ESRF - The European Synchrotron, 38000 Grenoble, France

Department of Materials, Henry Royce Institute, University of Manchester, Manchester, UK

A. Cohen
Department of Mechanical Engineering, Ben-Gurion University of the Negev, 84105 Beer-Sheva, Israel

A. Cosculluela
CEA-CESTA, 33114 Le Barp, France

1 Introduction

Predicting the fracture behavior of ceramics under high-speed impact conditions remains a challenge. Ceramic materials are of significant interest for many applications related to the protection of equipment and personnel. Compared to metallic and polymeric materials, ceramics exhibit improved fracture properties at very high strain rates, while maintaining these properties at elevated temperatures. Diagrams showing the evolution of maximum tensile stress indicate an increase at very high strain rates. Analytical and numerical models can predict this evolution. Micromechanical models attempt to explain this increase in maximum stress at very high speeds by considering the interaction between damage development in heterogeneities and mechanical stress (Denoual and Hild 2000; Paliwal and Ramesh 2008; Longchamps 2024). Experimentally, it is very complex to access the small spatial and temporal scales necessary to describe the damage mechanisms associated with the microstructure. Therefore, obtaining experimental evidence to

Published online: 13 January 2025

validate the simulation results derived from micro-mechanical models is difficult. At the very least, the properties at fracture can be rigorously estimated.

It is generally accepted that the fracture properties of ceramics depend on strain rate and/or crack velocity (Freund 1998). The evolution of fracture properties can be estimated from experiments on notched or unnotched geometry. Without notching, the evolution of the material's stress at fracture as a function of the loading regime can be used to explain the strain rate sensitivity of fracture properties (Belenky and Rittel 2012). With notching and for a brittle material, the Linear Elastic Fracture Mechanics (LEFM) formalism can be applied. Fracture energy (G_c) (Vekinis et al. 1990) and/or fracture toughness (K_c) (De Aza et al. 2002; Sawaki et al. 1993) are generally estimated experimentally, usually in mode I. In order to study the sensitivity to the loading regime, the crack velocity is generally taken into account. The Rayleigh wave velocity is a key indicator of the cracking regime. Theoretically, c_R represents the maximum allowable crack velocity. However, Yoffe (1951) has shown that above $0.6c_R$ the crack can branch for inertial reasons. This has since been confirmed experimentally for many materials (Ravi-Chandar and Knauss 1984; Kopp et al. 2014).

Few geometries are available in the literature to study the fracture properties (strip band specimen (Popelar and Atkinson 1980), compact tension (Beguelin et al. 1998), double cantilever beam (Robinson and Song 1992)) of brittle materials such as ceramics under dynamic loading. Compression tests using impact systems can be used to generate tensile stress in some specimens and therefore mode I. The difficulty often lies in locating and isolating a single crack in order to apply the LEFM. The modified brazilian test has been used for brittle materials such as rocks (Thiercelin and Roegiers 1988; Tutluoglu and Keles 2012) or pharmaceutical tablets (Croquelois et al. 2021). Due to its cylindrical geometry, this test can be easily adapted to dynamic test equipment such as *split Hopkinson compression bars* (SHPB) (Scapin et al. 2017). Duplan et al. developed the Rockspall test (Duplan 2020). The spatio-temporal data of the crack tip was tracked using a ultra high speed camera and the calculated velocities are of the order of $0.8c_R$. However, due to the non-symmetrical positioning of the notch and the so-called tilting effect, a plausible explanation for the measured cracking velocity greater than $0.6c_R$ may be the presence of a mixed failure mode I+II.

For crack regimes $\dot{a} > 0.1c_R$, the inertial effects associated with rapid crack propagation must be taken into account when estimating fracture properties. Some of the available energy is converted to kinetic energy and is therefore not consumed by the crack as it propagates (Freund 1998; Anderson 2017; Nilsson 1972). There are several approaches to take into account of this phenomenon, but the most widely used recommends applying a dynamic correction factor to the fracture properties (G_c and K_c) which evolves linearly with the crack velocity (Broberg 1960). However, it does not take into account the geometry of the specimen and therefore the associated wave reflections. A more rigorous method is to use numerical simulation to analyse the experimental data. Generation phase simulation method has been tested for a number of geometries (Nishioka 1997). The analysis reveals that, with a strip sample, Broberg's solution overestimates the correction at $0.6c_R$, whereas with a modified Brazilian sample, it considerably underestimates it (Croquelois et al. 2021).

In this work, *Split Hopkinson Pressure Bars* (SHPB) experiments were conducted using a modified Brazilian test on several grades of porous Al_2O_3 ceramics to localize crack initiation and study crack propagation. Ultra-high-speed X-ray phase contrast imaging, empoying synchrotron radiation at the ID19 beamline of the European Synchrotron Radiation Facility (ESRF), was used to capture the dynamic propagation of the crack. This technology enables through-volume measurement of the initiation of a single crack (Rubio Ruiz et al. 2024) at the level of the defect introduced into the sample, ensuring that no secondary damage occurs during the propagation of the crack of interest. The in situ data analysis facilitated the identification of the crack path and fracture energy, while inertial effects were accounted for using a direct numerical simulation approach, validated against the analytical solution proposed by Broberg (1960). The materials studied include several grades of porous Al_20_3 ceramics. The results provide valuable insights into the influence of porosity on the evolution of dynamic fracture properties, addressing a gap in the literature where data on porous ceramics is limited.

2 Materials and methods

2.1 Dense and porous alumina

Four different types of aluminas Al_2O_3 were manufactured by the Galtenco Solution company using a gel-casting process (Gaüzère et al. 2023): one dense and three porous grades. Among the porous grades, two exhibit 20% of porosity at either the micro (20micro) or mesoscale (20meso), while the third porous grade has 60% porosity at the mesoscale (60meso). The main process information regarding the different sample types is summarized in the Table 1. The resulting structure of the different sample is presented in Fig. 1. More detailed information regarding the porous structure and its link with the quasi-static compressive behaviour can be found in a previous published work (Henry et al. 2024).

2.2 Dynamic fracture experiments

Studying the tensile mechanical properties of brittle materials, such as concrete (Carneiro 1943; Garcia et al. 2017), rock (Belrhiti et al. 2017; Fairhurst 1964), pharmaceutical tablets (Mazel et al. 2016; Croquelois et al. 2021) or even ceramics, Scapin et al. (2017) presents several challenges. These challenges stem from difficulties in sample preparation and alignment, as well as early fracture occurring within the dies during direct tensile testing (Chen et al. 2013). To overcome these issues, indirect tests such as the Brazilian test (Wang et al. 2004) or the modified Brazilian test (Thiercelin and Roegiers 1988) are commonly used to estimate tensile properties.

2.2.1 Modified Brazilian test

In the modified Brazilian test, a cylindrical sample is subjected to compressive forces along its diameter, which induces tensile stresses at the center of the specimen through the Poisson effect. Because ceramic materials exhibit an asymmetric tension-compression response, the tensile stresses at the center are assumed to cause fracture. The elastic theory in a 2D plane stress framework shows that the maximum tensile stress occurs at the center of the specimen under the assump-

Table 1 Manufacturing parameters and characteristics of alumina samples

Sample	Sintering temperature (T_s)	Sintering time (t_s)	Porosity	Method to introduce porosity	Type of porosity
Dense	1530°C	9h	0.01 ± 0.01	–	Interstitial
20 micro	1400°C	3h	0.21 ± 0.01	Under sintering	Microporosity
20 meso	1530°C	3h	0.22 ± 0.01	Polymer preforms	Spherical mesoporosity
60 meso	1530°C	3h	0.61 ± 0.01	Polymer preforms	Spherical mesoporosity

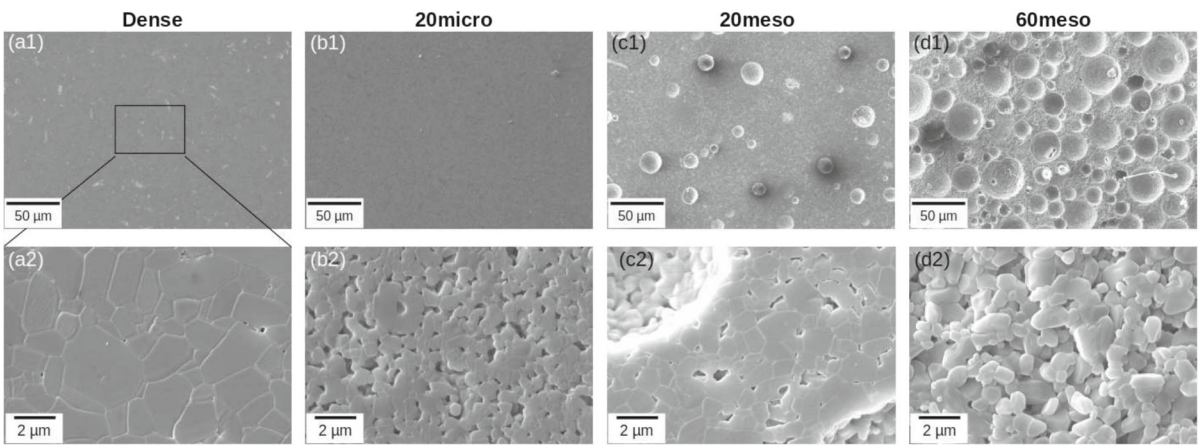

Fig. 1 Scanning electronic microscopy (SEM) observation of the microstructure of dense (**a**), 20micro (**b**), 20meso (**c**) and 60meso alumina (**d**). The Figures in the second row (x20 000) is a magnification of the first row (x1000)

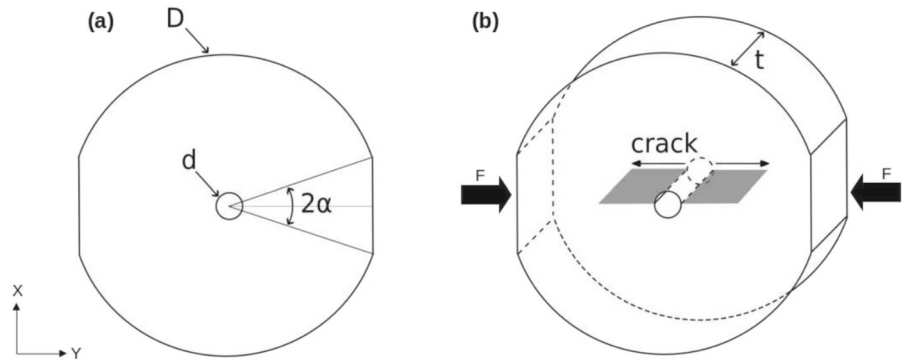

Fig. 2 Geometry of modified Brazilian specimen with platens and hole in the center (**a**), crack propagation in modified Brazilian test (**b**)

tion of elastic behavior (Belrhiti et al. 2017; Scapin et al. 2017).

However, interpreting the results of the Brazilian test can be complex. Previous studies have shown that cylindrical geometries do not always guarantee central fracture during diametral compression tests, due to stress concentration near the poles of the sample (Mazel et al. 2016; Chen et al. 2013; Wang et al. 2004). To address this, a flattened geometry has been proposed to ensure a more homogeneous and constant zone of tensile stress at the center of the sample (Mazel et al. 2016). However, this modification leads to an overestimation of the stresses that needs to be taken into account.

Addiotionaly, Hiestand et al. (1977) proposed to insert a circular hole of controlled size at the center of the specimen to concentrate stress at the edge, as shown in Fig. 2(a). A primary crack is then initiated at the edge of the hole and propagates toward the flat poles of the sample, parallel to the loading axis (Fig. 2b) (Croquelois et al. 2021). By varying the hole size, different crack initiation and propagation kinetics can be obtained. Croquelois et al. (2017).

The tensile stress σ_T is determined by the following equation 1 developed by Hobbs (1965) and improved by Wang et al. (2004) to take into account the effects induced by the flat poles.

$$\sigma_T = k(\alpha)\frac{P}{\pi D t}\left(6 + 38\frac{d^2}{D^2}\right). \tag{1}$$

where t is the thickness, D the outer diameter, d the inner diameter and P the load. However, the use of flat surface ensures a uniform tensile stress field at the center of the specimen in a conventional Brazilian test. The geometrical correction factor $k(\alpha)$ is applied to take into account the effect of the flat surfaces and avoid an overestimation of the tensile stress. Samples with a thickness $h = 4$ mm, diameter $D = 20$ mm and angle $\alpha = 11.5^o$ were used. According to Wang et al. (2004), for an angle $2\alpha = 23^o$, $k(\alpha)$ is 0.945.

For each ceramic grade presented above, a minimum of 4 to 5 specimens were tested to ensure reproducibility. The measurement dispersion, which reflects the inherent variability of the material properties was computed, as it has a more significant impact on the results than the experimental uncertainty, given the probabilistic nature of alumina fracture behaviour.

2.2.2 *Split Hopkinson pressure bar (SHPB) experimental setup*

A Split Hopkinson Pressure Bar setup was used to impose a dynamic loading conditions (Chen and Song 2010). Knowing the incident, reflected and transmitted strains at their measurement points, it is possible to calculate the force applied to the faces of the sample using Koslky post-processing (Kolsky 1949; Chen and Song 2010).

$$\begin{cases} F_1 = S_b E_b(\epsilon_i + \epsilon_r) \\ F_2 = S_b E_b(\epsilon_t) \end{cases} \tag{2}$$

where S_b is the section and E_b the Young's modulus of bars (Fig. 3). Given the special geometry of the sample, it will be difficult to obtain a balance of forces. This is why, according to Asadi et al. (2022), the average force is taken to be:

$$F_{ave} = S_b E_b \epsilon_t \tag{3}$$

The bars and projectile are made of high-strength 42CD4 steel. The mechanical properties and dimen-

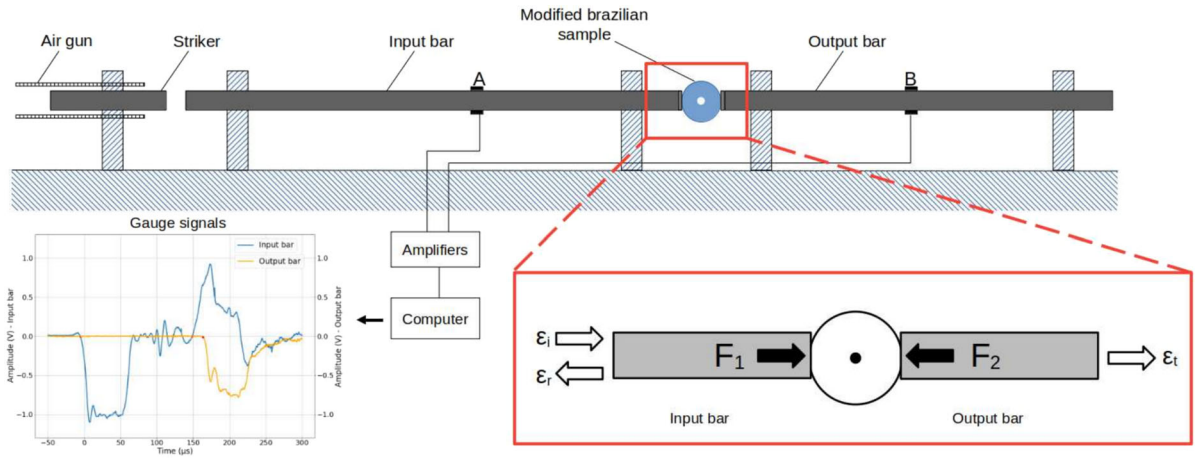

Fig. 3 Scheme of the split Hopkinson pressure bar for dynamic modified Brazilian test

Table 2 Dimensions and properties of the bars in the SHPB device

Density (kg/m^3)	8100
Young's modulus (GPa)	210
Poisson's ratio	0.3
Input bar length (mm)	1400
Striker length (mm)	150
Bars and striker diameter (mm)	12.7
Wave velocity c_0 (m/s)	5172

sions are detailed in the Table 2. The specimens were diametrically compressed by interposing small disks of hardened steel to avoid indentation of bar faces. No pulse shaper was used for tests.

Typically when the SHPB are used to determine uniaxial compressive response of bulk material, strain rates in the range 10^2 s^{-1} to 10^4 s^{-1} can be achieved. However, given the complex geometry of the sample, the strain field is highly inhomogeneous, making it impossible to calculate a strain rate. It is however possible to estimate a constant loading rate $\dot{\sigma}$ (MPa s^{-1}). This loading rate will be equal to the slope of the linear part of the "stress vs time" curve (Li et al. 2016; Chen et al. 2014).

2.2.3 *Single-bunch synchrotron X-ray phase contrast radioscopy*

Experiments were performed exploiting the single-bunch imaging capabilities on ID19 beamline and a SHPB setup available through the user experiment program.

During the experiments, the ESRF operates with 16 bunch filling mode (Chapman et al. 2024) providing a continuous train of bunch electrons with 176 ns time spacing and pulse width of about 60 ps (FWHM). The X-ray pulses of equivalent time spacing are produced by two axially aligned long period undulators ($\lambda = 32$ mm) set to minimum gap (11.5 mm). The experimental set-up is located in the beamline experimental hutch approximately 145 m downstream from the source having the detector placed at about 9 m downstream from the sample (Fig. 4a). This ensures that the recorded images are within the propagation-based phase contrast regime (Olbinado et al. 2017).

The transmitted beam is encoded using an indirect ultra-high speed detector assembly consisting of two HPV-X2 (Shimazu, Japan) ultra-high speed cameras, equiped with 1X tandem lens (50:50 mm AF-2 Nikkor f/1.4) coupled to a 500 μm LYSO:Ce fast-decay scintillator (about 40 ns) (Lukić et al. 2021). The camera sensor has 400 x 250 effective pixels count with a nominal pixel size of 32 μ m and on-board memory able to store 128 full frames in a single burst imaging mode and each camera records images with a frame rate equal to 1.8 Mfps (Fig. 4b). These two ultra-fast cameras record images in staggered order, giving a total of 256 images and an frame rate of 3.6 Mfps. As a result of the entire optical arrangement, a very large field of view of 12.8 $\times$ 8 mm^2 (Fig. 4d) is captured within each radiograph providing the ability to study various

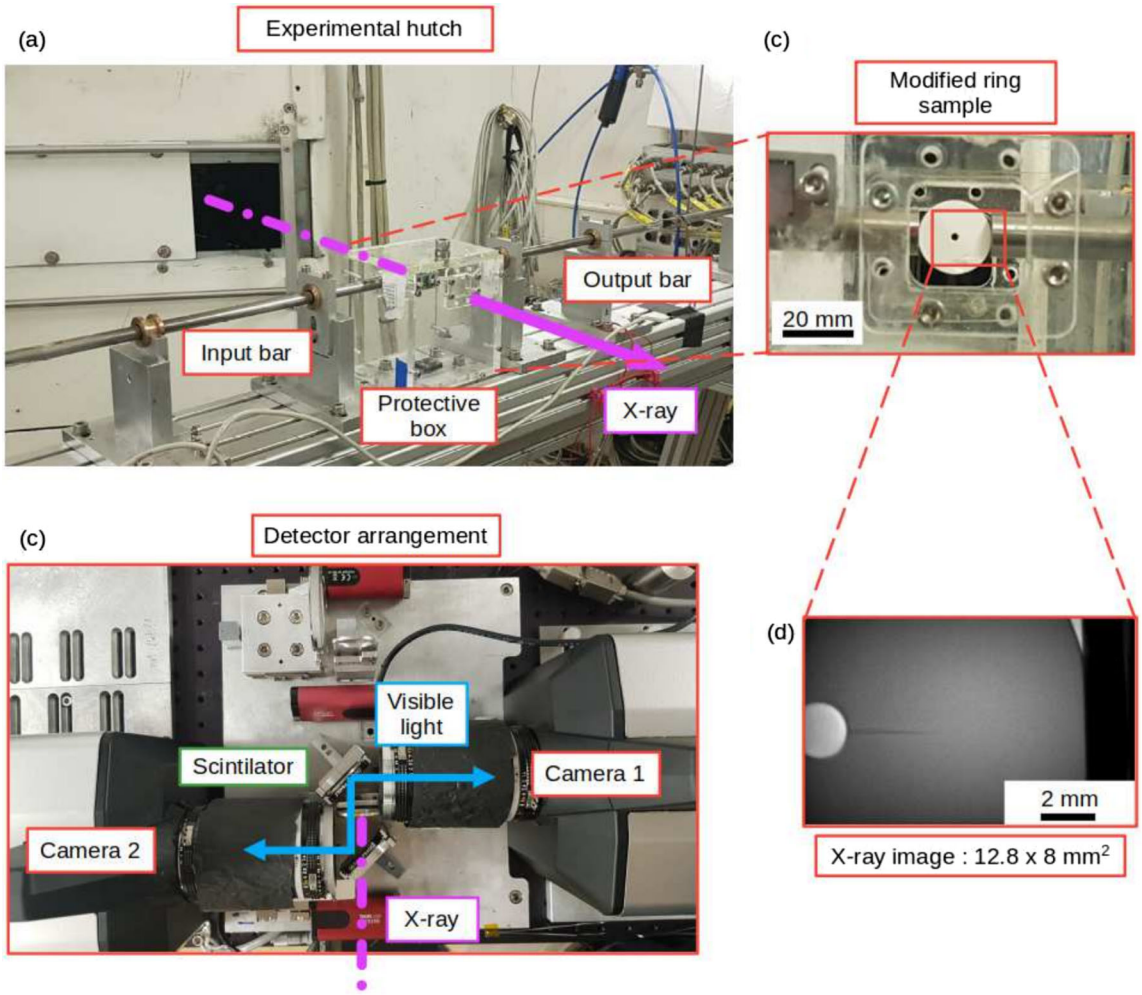

Fig. 4 Experimental SHPB setup at ID19: beamline hutch and optical arrangement of the ultra-high speed indirect detector system

transient dynamic phenomena within a representative volume scale. As illustrated on the Fig. 4d, the very large field of view ($12.8 \times 8\ mm^2$) allows observation of the propagation of the first main crack from the edge of the hole to the flat pole.

2.3 Dynamic fragmentation and post-mortem fragment analysis

By taking advantage of the combination of ultra-fast imaging and X-ray radiography, it is possible to observe the initiation and propagation of cracks in the volume. A main crack is observed to propagate first, followed by secondary cracks as the main crack reaches the end of the sample. The Fig. 5 illustrates the main initiation crack propagated from the hole to the flattened pole of the sample for all shades of alumina. Depending on the density of the sample, the X-rays are more or less attenuated by the sample, leading to images with varying degrees of contrast. In the case of dense alumina, the images are very high contrast, making it easy to follow the propagation of the crack (Fig 5a). Conversely, for highly porous aluminas, image analysis steps will be necessary to highlight the crack (Fig 5d).

Fig. 6 illustrates the damage kinetic of a modified Brazilian sample. Secondary cracks initiate and propagate once the main first crack has stopped near the flat ends (Fig. 6c, d). These secondary cracks start at the end of flattened poles on either side of the sample and propagate to the center of the sample where they

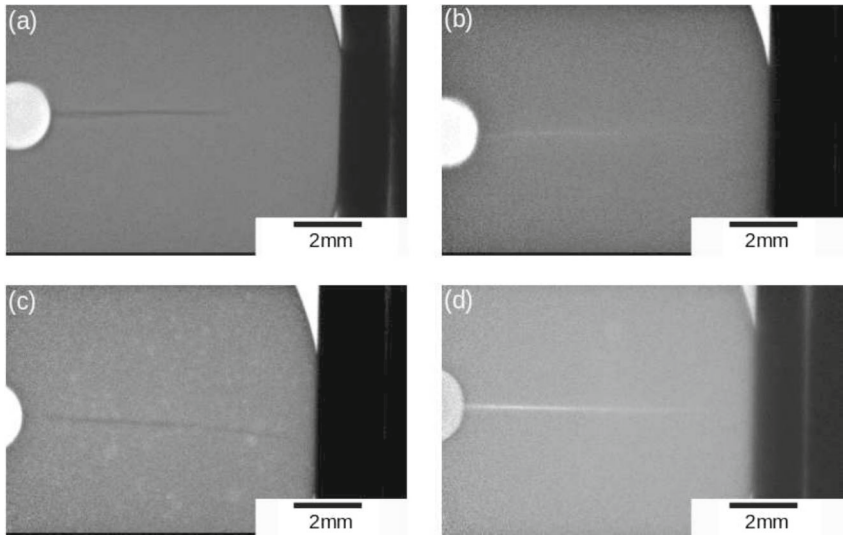

Fig. 5 Raw *in situ* X-ray radiographs of rapid crack propagation in dense (**a**), 20micro (**b**), 20meso (**c**) and 60meso (**d**) alumina

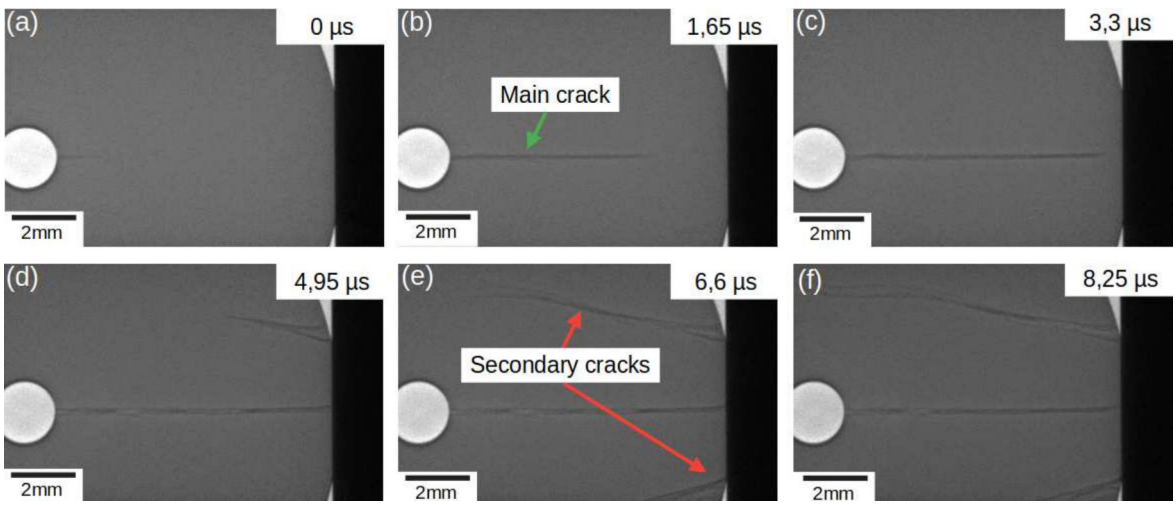

Fig. 6 Fragmentation phenomena during a dynamic modified Brazilian test on a dense alumina

coalesce and finally propagate to the hole (Fig. 6d, e, f).

The recovered fragments were used to identify the surface related to the main crack (Fig. 7a). The fracture surfaces associated with the main initiation crack were analyzed by scanning electron microscopy in order to highlight the local fracture mechanisms (red square in the Fig. 7a). In order to highlight the different fracture mechanisms between initiation and propagation at a constant crack velocity, fracture surfaces were observed close to the hole (initiation zone) and at the center of the surface (Fig. 7b). For all tested sample configurations analysis was performed with 100X and 1000X magnification, outlying different scales of fracture surface microstructural characteristics.

2.4 Finite element modeling of dynamic fracture

A numerical procedure for analysing the experimental data is implemented. Finite element modeling (FEM) was used to estimate the inertial correction of the dynamic energy release rate (G_{Id}) induced by a rapid crack propagation in the modified brazilian sample. The numerical procedure consists in predicting the structure behaviour during rapid crack propagation and analyzing experimental data to estimate the dynamic frac-

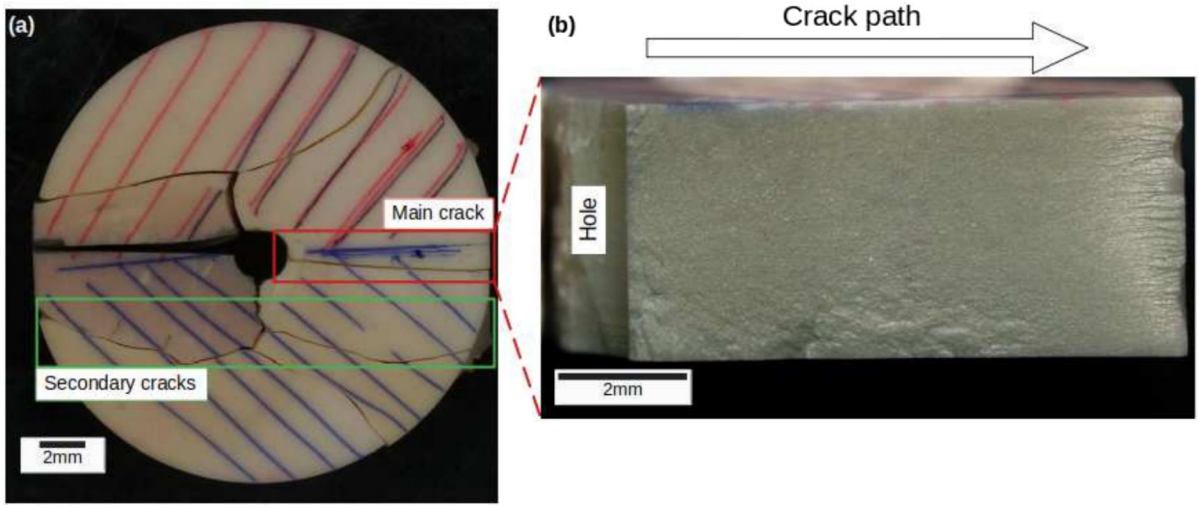

Fig. 7 Recovered fragments from a dense sample (**a**), Surface witnessing the propagation of the main crack (**b**)

ture energy (G_{ID}). *By isolating a single crack, whose loading and propagation conditions are known, it is therefore possible to apply the LEFM formalism to estimate the fracture energy* G_{ID}. The potential dynamic effects associated with impact via the Hopkinson bars were considered to be negligible compared with those induced by the rapid crack propagation. The dynamic fracture mechanism was computed thanks to a generation phase simulation and a node release technique was implemented (Kopp 2013; Arthur Core et al. 2018). The fracture criteria is the spatio-temporal data of the crack tip $\dot{a}$ during dynamic propagation. This model has been already validated using the analytical solution of Broberg (1960), for a crack propagation in a semi-infinite plate in mode I at different crack velocities (from 0.01 to $1c_R$) (Croquelois et al. 2021). The numerical model allows to estimate the dynamic correction factor by taking into account inertia effects induced by the rapid crack propagation.

For the simulations, the different grades of porous alumina ceramics were considered as isotropic elastic materials. For each type, the value of the Young's modulus and the Poisson ratio were taken from preciously published results (Henry et al. 2024). Exploiting the axisymmetry of the problem, only one eighth of the modified brazilian numerical sample was modeled. The 3D finite element mesh used 8-nodes hexahedron elements, as can be seen in the Fig. 8. This particular mesh has already proved to be very reliable for simulating dynamic fractures (Kopp et al. 2014). For this

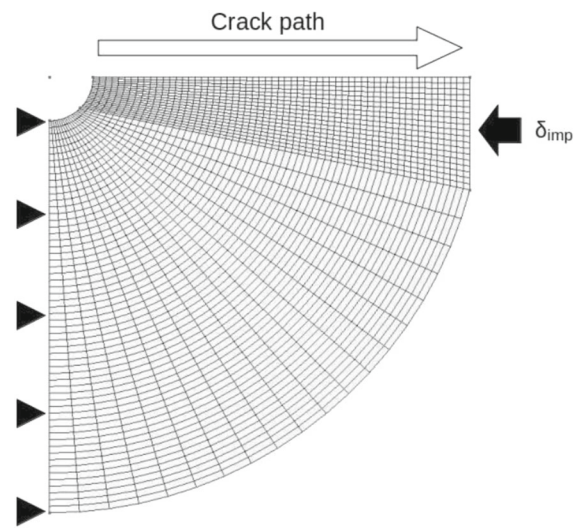

Fig. 8 Mesh used for modified Brazilian simulation

simulation, 60 elements are regularly spaced along the crack path along the Y direction and 5 elements are placed in the thickness. The numerical method used in this simulation consists of solving a Newmark problem with parameters $\alpha = \beta = 1/2$, which corresponds to solving an implicit problem (Wilson and Bathe 1976).

The sample is loaded in compression by applying a controlled displacement at the flat ends. The displacement value was chosen to generate a force on the sample equal to the experimental mean fracture force. Only the dynamic effects induced by rapid crack propagation

were taken into account in the numerical analysis of the results. It has been shown that the stress fields between the quasi-static regime and the dynamic regime are similar in CT fracture tests (Beguelin et al. 1998), which is why the dynamic effects induced by SHPB loading have been considered negligible compared with the fracture dynamics.

After a first static solving of the problem, the displacement at the flat ends was fixed. Then an explicit dynamic solver was used to propagate the node opening along the vertical symmetry plane (Fig. 8). The nodal release velocity (in % of c_R) was imposed constant. As the boundary condition at the crack path in this simulation is a symmetry one, the nodal release is done by cancelling this boundary condition at the nodes where the crack appears.

3 Experimental results

3.1 Influence of the porosity on the dynamic mechanical response

Typical raw signals measured by strain gauges placed on the input 400 mm from the specimen and output bars are shown in Fig. 9a for the case of dense alumina sample. The variations of the incident, reflected and transmitted signals are represented in Fig. 9b. Figure 9c shows the typical variations of input and output forces calculated from the data of the Fig. 9b using equation 2. The good overlap between the input and output forces indicates that an equilibrium state in the specimens was reached during the dynamic loading. Since dynamic equilibrium was reached before the fracture, only the output force is used in the rest of this work.

Thanks to the presence of the hole in the center of the samples, the crack propagated almost simultaneously on either side of the hole towards the flat poles of the sample. The variations in the tensile stress as a function of time (Fig. 9d) show an increase in the tensile stress up to a maximum corresponding to the initiation of the main crack at time t_0. The drop in tensile stress following the maximum tensile stress represents the propagation of the main crack. The variations of tensile stress σ_T versus time allow to determine the loading rate, which corresponds to the slope of this straight line, as shown in Fig. 9d.

Table 3 summerizes the average value of fracture force, *dynamic tensile strength* and loading rate for the four different materials. The *dynamic tensile strength* determined experimentally using the modified brazilian test is close to the values found in the literature (around 350 MPa) (Scapin et al. 2017; Ji et al. 2022; Zheng et al. 2023) in the case of dynamic loading. However, the geometry of the sample does not allow a constant deformation zone to be obtained, so it is not possible to estimate the Young's modulus.

The *dynamic tensile strength* decreased by increasing the pore volume fraction. These results follow the same variation as in a previous work (Henry et al. 2024) but it appears that the decrease in *dynamic tensile strength* as a function of porosity rate can be represented by linear regression. Moreover, the relative scatter of fracture force is quite dependent on the porosity fraction of the ceramic. It seems to decrease as the porosity fraction increases (Fig. 10). The scatter obtained for dense alumina is of the same magnitude as in the work of Scapin et al. (2017). The large error bars are due to the inherent nature of brittle materials and their probabilistic behaviour. As the tensile stress at failure is largely sensitive to intrinsic and extrinsic defects, it is common to observe this variability in the literature. Furthermore, at isodensity ($P \approx 20\%$), microporous alumina appears to be less resistant than mesoporous alumina. However, given the wide *scatter* of the results, it is difficult to conclude definitly on this observation.

3.2 Influence of the porosity on the crack velocity

Several samples per grade were tested and observed as shown in the Table 3. In order to remove the artefacts and highlight the crack that is propagating, a few image processing steps are required to highlight the crack. For each image of the crack propagation, the crack tip is characterised by a change in greyscale as in the Fig. 11. Indeed, the X-rays are partly attenuated and refracted as they pass through the sample, which allows the phase contrast method to highlight the crack. The use of the colour map in the Fig. 11 highlights the contrast between the shades of grey observed in Fig. 5, making it easier to observe the cracks and measure their length. The length of the crack is measured for each image of the crack propagation knowing that 1 px = 32 μm. The Fig. 11 represents the post-treated pictures captured by ultra-fast radiography during the

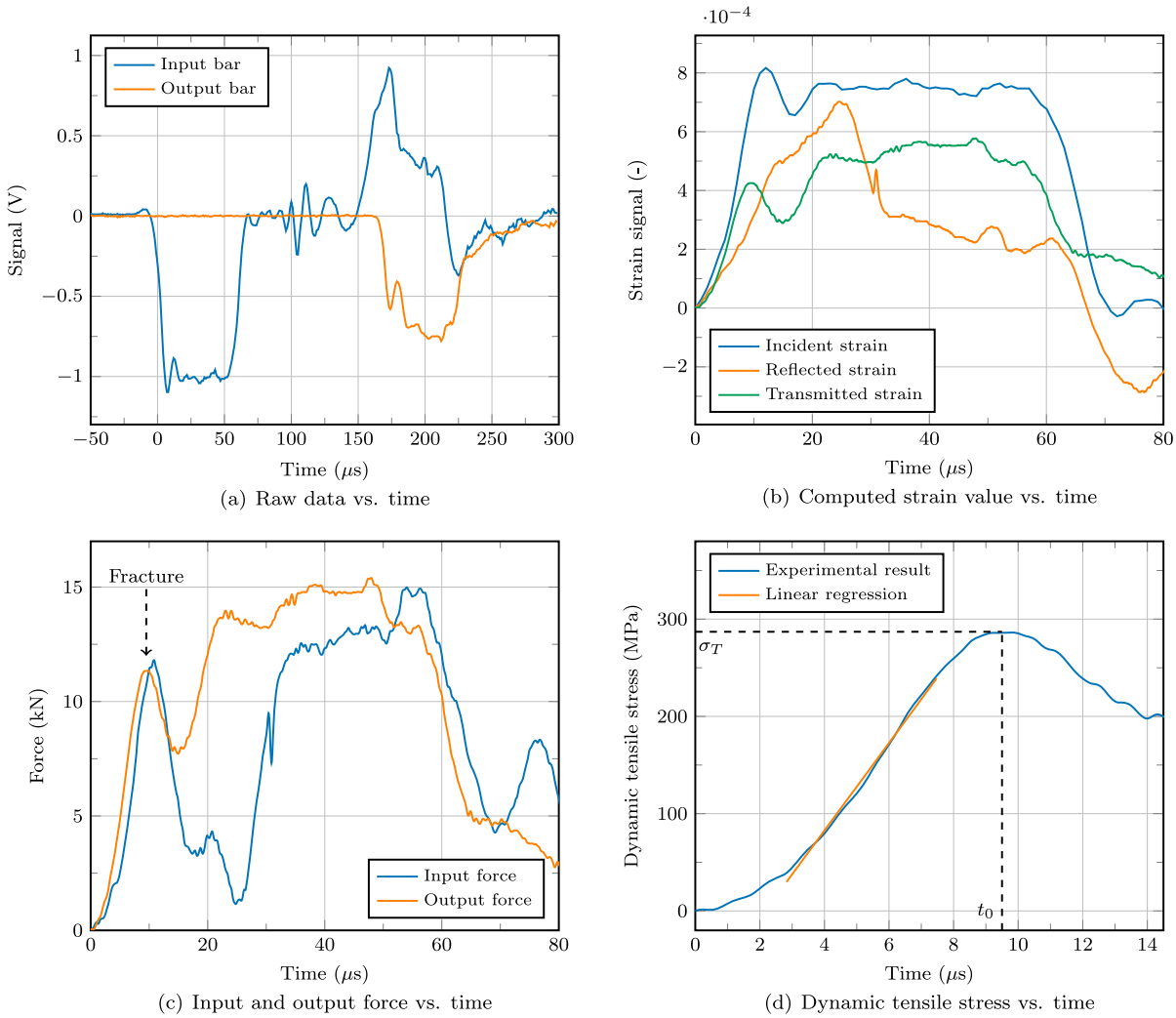

(a) Raw data vs. time

(b) Computed strain value vs. time

(c) Input and output force vs. time

(d) Dynamic tensile stress vs. time

Fig. 9 Mechanical results for dense alumina obtained on SHPB apparatus

Table 3 Mean values of the fracture properties of porous alumina

Name	porosity rate	Fracture force (kN)	Fracture stress (MPa)	Loading rate (MPa.s^{-1})	Number of sample
Dense	0.01 ± 0.01	11.5 ± 3.4	304 ± 83	45 ± 19	4
20 *micro*	0.21 ± 0.01	9.3 ± 2.2	221 ± 78	36 ± 18	5
20 *meso*	0.22 ± 0.01	12.1 ± 3.8	249 ± 75	40 ± 14	5
60 *meso*	0.61 ± 0.01	5.6 ± 0.8	137 ± 44	23 ± 5	5

rapid crack propagation in modified brazilian sample tested under dynamic regime for all shades of alumina.

By using two separate cameras (Cam1 and Cam2 on the Fig. 12a), the length of the crack can be accurately determined. The time t_0 is chosen like reference point where the crack begins to propagate in dynamic state (Fig. 9d). Considering the frame rate of each camera (1.8 Mfps) and the delay between the first camera and the second (176 μ s), it is possible to plot the evolution of the crack tip location as a function of time. Initially,

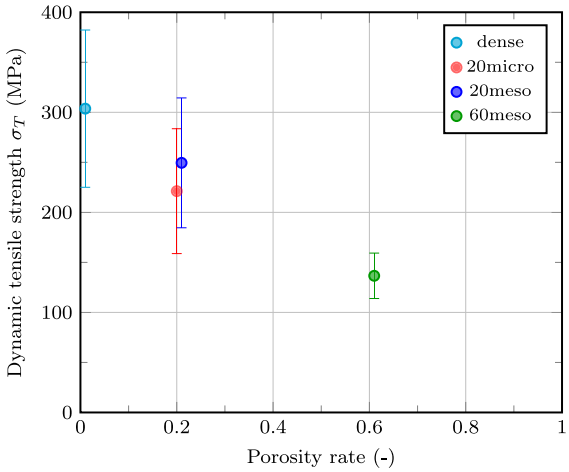

Fig. 10 Dynamic tensile strength (MPa) vs. porosity rate

the crack initiates from the hole and first accelerates (points A and B), then propagates (points B to G) at a relatively constant velocity $\dot{a}$ (Fig. 12b). Due to the compression field near the flat surfaces (Scapin et al. 2017), the crack slows down and stops, as shown in the Fig. 12b at point H. The propagation velocity measured for the different grades of alumina are shown in the Table 4.

Fig. 13 shows the crack tip position as a function of time for all alumina grades. The crack velocity is determined by linear regression and listed in Table 4. The relative error associated with each velocity is between 10 and 20% and increases as the porosity fraction increases. There are likely more irregularities and variations in the material structure.

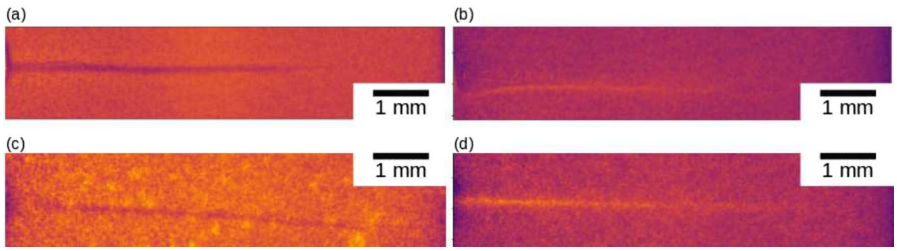

Fig. 11 Post-processed images of rapid crack propagation in dense (**a**), 20micro (**b**), 20meso (**c**) and 60meso (**d**) alumina

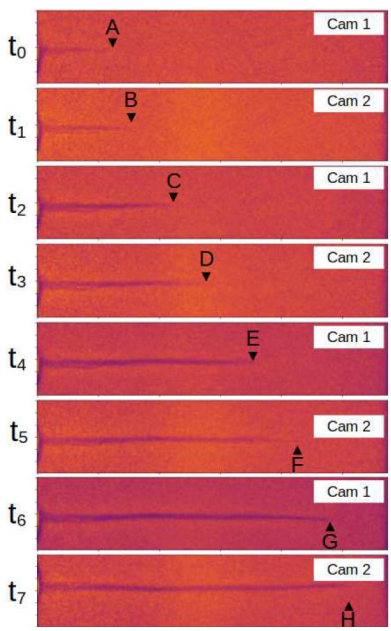

(a) Crack tip position.

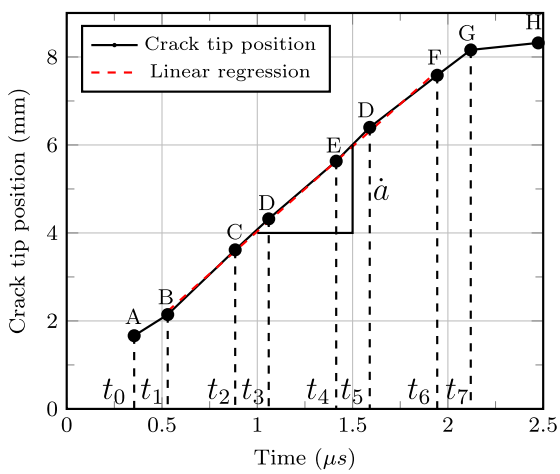

(b) Crack tip length vs time.

Fig. 12 Rapid crack propagation in a dense alumina (dense) brazilian sample observed with at 3.6 MHz. Time t_0 is the reference point where the crack begins to propagate. At time t_7 the sample is completely fractured (**a**) and the crack position versus time is plotted and fitted with a linear regression $f(x) = \dot{a}x + b$ with $\dot{a} = 3.86$ km/s (**b**)

Table 4 Crack velocities for the different porous alumina

Name	Crack velocity (km/s)	Coefficient of variation (%)	c_R (km/s)	$\dot{a}/c_R$ (%)
dense	3.6 ± 0.3	6.3	5.7 ± 0.6	64 ± 10
20*micro*	3.2 ± 0.3	6.5	5.0 ± 0.5	64 ± 10
20*meso*	3.0 ± 0.3	8.9	5.0 ± 0.5	60 ± 10
60*meso*	1.7 ± 0.4	21.3	3.8 ± 0.4	45 ± 10

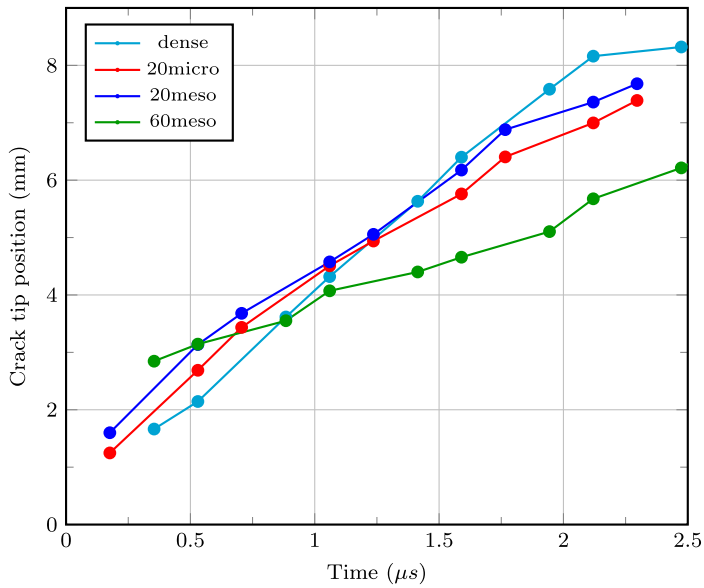

Fig. 13 Crack position versus time for all alumina grades

The crack velocity is commonly expressed as a function of the Rayleigh wave velocity c_R. Rayleigh wave velocity (m/s) is expressed as a function of density ρ, Poisson's ratio ν, shear modulus $\mu = \dfrac{E}{2(1+\nu)}$ and transverse wave velocity c_T (Kopp et al. 2014). These parameters and the Young's modulus E were determined in a previous work (Henry et al. 2024).

$$c_R = (0.874032 + 0.200396\nu - 0.00756704\nu^2)c_T$$
$$with \quad c_T = \sqrt{\frac{\mu}{\rho}}. \tag{4}$$

The Rayleigh wave velocity (Eq. 4) will therefore be determined for each grade of alumina, by assuming them, to a first approximation, to be homogeneously isotropic. Given the random nature of the pores dispersion (Henry et al. 2024), these aluminas can be considered isotropic.

The $\dot{a}/c_R$ ratio for the different grades of alumina is given in the Table 4. The cracking velocity seems to reach the upper limit of 60% of Rayleigh wave speed c_R with a scatter of 8% for dense, 20meso and 20micro aluminas. For the most porous grade 60meso, the crack velocity reaches only 45 ± 11 % of the Rayleigh wave speed. No branching was observed during the main propagation, which suggests that the cracking velocity is effectively less than or equal to $0.6c_R$ assuming that all previous research considers this to be the maximum velocity. It would appear that the maximum velocity is reached in mode I for 3 grades of alumina.

In the end, it was observed that the artificial defect, as desired, localised the crack initiation regardless of the grade tested. During rapid propagation, a mode I is revealed by the rectilinear trajectory and no macroscopic branching is observed despite the high propagation speed. At the velocities reached, the porosities could have acted as local field disruptors during the rapid propagation, which could have affected the trajectory of the crack and possibly caused it to branch off. The influence of porosity on these aspects is therefore minor. However, porosity has a significant influence on crack velocity.

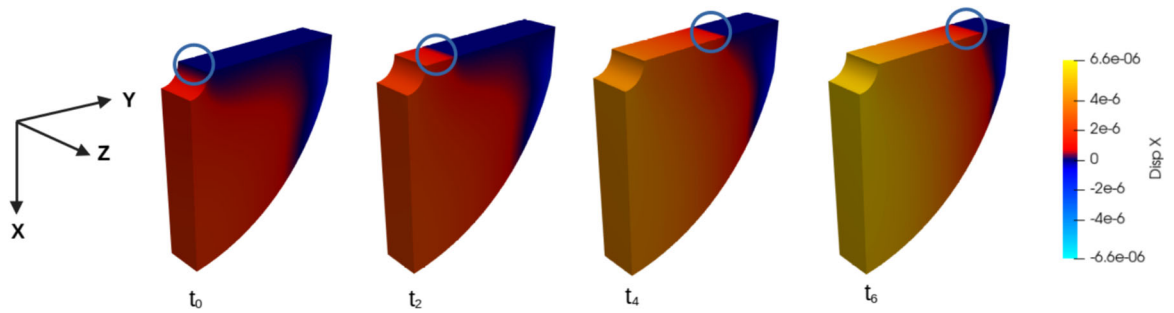

Fig. 14 Numerical crack propagation: node release technique resulting displacement field along the X axis for $\dot{a} = 0.6c_R$. Crack tip is highlighted by red circles

4 Estimation of the dynamic energy release rate G_{Id} using FEM simulation

4.1 Numerical rapid crack propagation

As mentionned, the propagation of the crack is represented by the cancellation of the Dirichlet boundary conditions on the last row of blocked nodes. These nodes are then free to move in the X direction to represent the crack opening. The Fig. 14 represents the displacement field along the X direction induced by the dynamic crack propagation at $0.6c_R$. 4 images represent the displacement fields along the X direction at different times. Dark blue represents zero displacement, while red and yellow represent positive displacement. The tip of the crack is defined by the dark blue end and the crack propagates at constant velocity as expected.

4.2 Energy balance during crack propagation

A method to estimate the energy release rate during a crack propagation regime is to perform an energy balance on the whole structure (Griffith 1921). This method can be used directly in a finite element simulation to estimate the dynamic energy release rate G_{Id} (Kopp 2013; Croquelois et al. 2021; Doitrand et al. 2022). Unlike the local contour integral method, this method does not require any local refinement of the mesh around the crack tip. A differential calculation is made between two crack tip locations a and $a + \Delta a$ which correspond to two successive sets of nodes of the finite element mesh along the crack path. This differential calculation does not therefore require any specific treatment of the singularity. The dynamic energy release rate G_{Id} is calculated such as:

$$G_{Id} = \frac{W_{ext} - \Delta E_{ela} - \Delta E_{kin} - \Delta E_d}{B\Delta a} \tag{5}$$

where W_{ext} is the work of the externals forces equal to zero during the crack propagation, ΔE_{ela} is the variation in elastic strain energy, ΔE_{kin} is the variation in kinetic energy, ΔE_d is the variation in numerical dissipated energy and B is the thickness of the sample. The last dissipative term, ΔE_d, is introduced as a numerical damping parameter to stabilise the potential oscillations due to the sudden opening of the nodes. This dissipation has no physical meaning and is not representative of the LEFM. It is therefore necessary to check that this term is not an influential source of energy dissipation. The total energy dissipated is, in this case, negligible compared with the other energies, as shown in Fig. 15(b), where the resulting energy balance for two cracks of $0.01c_R$ and $0.6c_R$.

Figure 15a shows the variation of the incremental energies ΔE_{ela}, ΔE_{kin} and ΔE_d as a function of the crack length for a very slow crack velocities ($\dot{a} = 0.01c_R$) where inertia effects are negligible. The elastic energy ΔE_{ela} increases with the length of the crack, reaching a maximum value between 60 and 80% of the maximum crack length (L). After that maximum, the elastic energy decreases significantly due to edge effects.

4.3 Influence of cracks velocities

The specific geometry of the specimen creates a zone of compressive stress close to the poles, preventing a stabilised cracking regime. The energy release rate

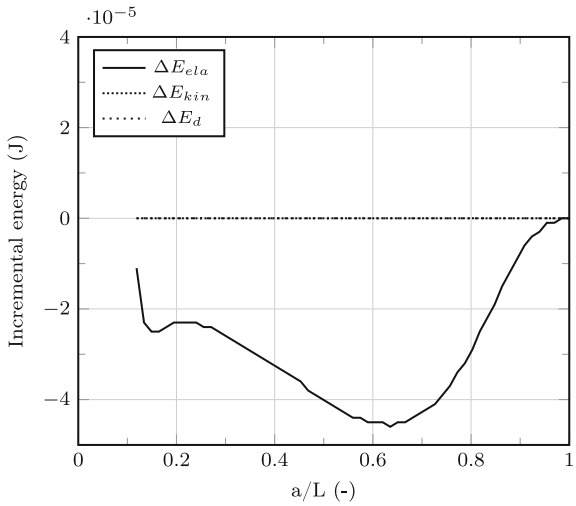

(a) Energy balance during crack propagation for $\dot{a}/c_R = 0.01$.

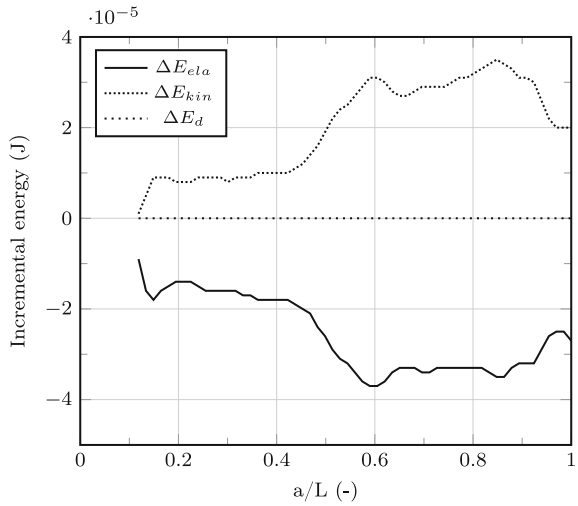

(b) Energy balance during crack propagation for $\dot{a}/c_R = 0.6$.

Fig. 15 Energy balance during crack propagation for $\dot{a}/c_R = 0.01$ (a) and $\dot{a}/c_R = 0.6$ (b)

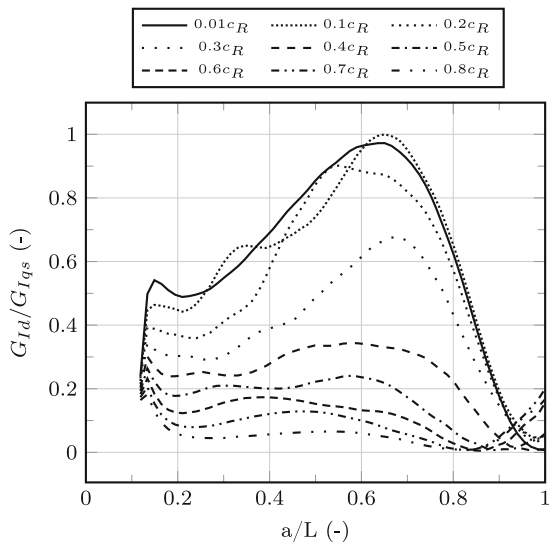

(a) Evolution of G_{Id}/G_{Iqs} according to a/L, with a the crack length and L the total crack length

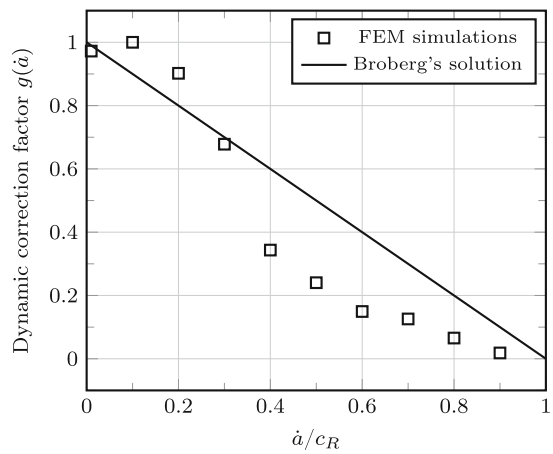

(b) Dynamic correction factor $g(\dot{a})$ vs. $\dot{a}/c_R$.

Fig. 16 Variation of G_{Id}/G_{Iqs} ratio as a function of a/L, with a the crack length and L the maximum crack length (**a**) and "Dynamic correction factor" vs. crack velocity for a crack opening in a flattened Brazilian disk with a hole (**b**)

increases as the crack propagates until it reaches a maximum value, then decreases when the crack reaches the zone of compressive stress (Thiercelin and Roegiers 1988). The fracture energy G_{Iqs} for a slow crack velocity ($0.01c_R$) was estimated using the maximum of the energy release rate curve. The variation of ratio G_{Id}/G_{Iqs} has been computed for several different crack velocities (from 0.01 to $1c_R$) and represented in Fig. 16a. For all crack velocities, the energy release rate increases with crack length until it reaches a maximum value between 50 and 70% of the maximum crack length (depending on the crack velocity) and then decreases significantly. The curves obtained are similar

Table 5 Dynamic factor correction $g(\dot{a})$ and dynamic fracture energy G_{IC} for porous alumina

Name	G_{IC} (Jm^{-2})	$\dot{a}/c_R$ (-)	$g(\dot{a})$ (-)	$G_{ID\ num}$ (Jm^{-2})	$g(\dot{a})_{bro}$ (-)	$G_{ID\ bro}$ (Jm^{-2})
dense	149	0.64 ± 0.08	0.15	22	0.4	60
20micro	63	0.64 ± 0.08	0.15	9	0.4	25
20meso	40	0.60 ± 0.08	0.15	6	0.4	16
60meso	17	0.45 ± 0.11	0.30	5	0.55	9

to those obtained by Thiercelin and Roegiers (1988) for berea sandstone.

At a given crack length, the ratio G_{Id}/G_{Iqs} decreases significantly with increasing crack velocities due to the inertia effects of rapid crack propagation. A dynamic correction factor is introduced to take into account the dependence of the crack propagation velocity. The dynamic correction factor $g(\dot{a})$ is defined as

$$g(\dot{a}) = \frac{max(G_{Id})}{G_{Iqs}} \tag{6}$$

with $G_{Iqs} = max(G_{Id})$ for $\dot{a} = 0.01c_R$. The variation of $g(\dot{a})$ as a function of crack velocities shown in Fig. 16b does not follow the quasi-linear decrease in $1 - \frac{\dot{a}}{c_R}$ proposed by Broberg (1960). The dynamic correction fracture is higher than Broberg's prediction for $0 < \dot{a}/c_R < 0.3$ and inversely for the $\dot{a}/c_R > 0.3$. For the fracture velocities reached in this study, the dynamic correction factor calculated by the numerical method is always lower than that calculated by Broberg's theory (Tab. 5) that means the dynamic fracture energy is overestimated with this theory. In the case of dense alumina, the measured crack velocities is equal to $0.6c_R$ corresponding to $g(\dot{a}) = 0.15$. It means only 15% of the available energy is dissipated by the crack propagation and that 85% of available energy is consumed by inertia effects. The remaining energy available in the sample can be used to initiate and propagate post-peak secondary cracks, as observed on the recovered fragments (Fig. 7). The same numerical simulations were carried out for all grades of porous alumina (Table 4) using the material parameters of each grade as input data. The same variation in the dynamic correction factor was observed for all grades.

As shown in the literature (Freund 1998; Nilsson 1972; Broberg 1960), we observe a decrease in the dynamic correction factor as the crack velocity increases. However, the trend observed thanks to the results obtained by numerical simulation show a much faster decrease in the correction factor compared with the analytical solution.

4.4 Estimation of dynamic energy release rate G_{ID}

G_{Iqs} for dense ceramic is numerically estimated to 149.3 J/m^2 for a slow velocity ($0.01c_R$) and this value is assumed to be comparable to G_{IC} upper values described by Vekinis et al. (1990) where the values are between 40 and 120 J/m^2 (Vekinis et al. 1990). Fracture toughness (K_{IC}) is much more widely studied in the literature (De Aza et al. 2002; Singh and Shetty 1989; Tomaszewski et al. 2000; Bouras et al. 2008; Casellas et al. 2003). These values are used to estimate fracture energy, in particular for a plane strain test where the following relationship is verified:

$$G_{IC} = (1 - \nu^2)\frac{K_{IC}}{E} \tag{7}$$

where ν is the Poisson ratio and E the Young's modulus. These values make it possible to enrich the comparison with the data obtained in this work (see in Fig. 17).

Calculated G_{IC} for all porous alumina shades are reported in the Table 5. These results demonstrate that fracture energy G_{IC} is dependent on the porosity rate as highlighted in the literature (Hong et al. 2006; Jelitto and Schneider 2019; Deng et al. 2001). Variations in critical fracture energy G_{IC} are represented by a geometric model developed on the basis of Ashby's work and perfected by Jelitto and Schneider (Jelitto and Schneider 2019, 2020). The model shown in Fig. 17 takes closed porosities into account and corresponds to the following equation

$$G_{IC}(P) = G_{IC0}(1 - P^{2/3})(1 - P)^n \tag{8}$$

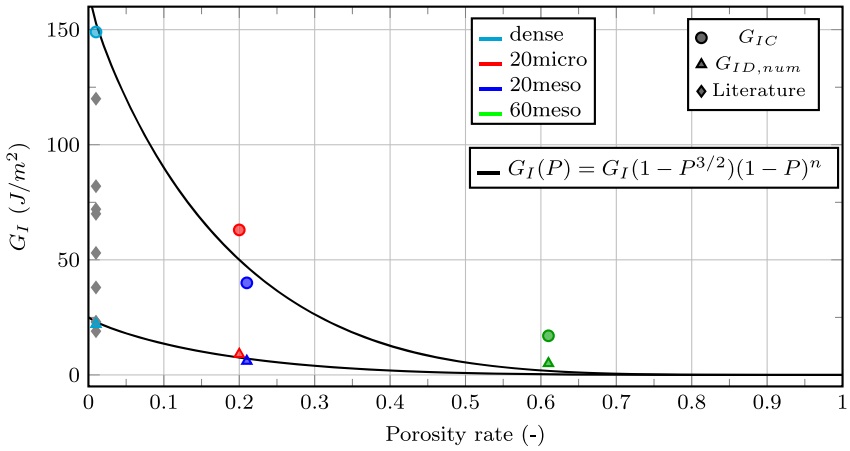

Fig. 17 Variation of critical fracture energy G_{IC} and dynamic fracture energy G_{ID} versus porosity rate

where G_{IC0} is the critical fracture energy for dense ceramic, P the porosity rate and n an adjusted exponent. In the case of this study, $n = 3.5$. The model reliably represents the evolution of the critical energy for low porosity rates (dense, 20meso) but seems to underestimate the fracture energy for high porosity rates (60meso). For high porosity rates, it is inevitable that interconnections appear between the pores until they lead to completely open porosity. It is then necessary to adjust or change the model accordingly. If the effects of inertia are not taken into account, the fracture energy G_{IC} of the material is overestimated. The dynamic correction factor $g(\dot{a})$ should be used to estimate the dynamic fracture energy G_{ID} as the following equation:

$$G_{ID} = g(\dot{a}) \times G_{Iqs} \tag{9}$$

As demonstrated previously, the value of the dynamic correction factor $g(\dot{a})$ depends on the crack propagation velocity $\dot{a}/c_R$. The dynamic correction factors associated with each crack propagation velocity are listed in Table 5. The dynamic correction factor increases as the crack propagation velocity decreases. This means that the proportion of energy dissipated by inertial effects decreases as the crack propagation velocity decreases. Similarly, the dynamic correction factor calculated by the Broberg theory $g(\dot{a})_{bro}$ and the associated dynamic fracture energy $G_{ID\,bro}$ are shown in Table 5.

The Table 5 and Fig. 17 show the evolution of the fracture energy G_{ID} calculated with FEM simulation and Broberg theory (Broberg 1960) as a function of the porosity rate. In the case of dense alumina with a crack velocity measured at $0.6c_R$, the value of the dynamic fracture energy G_{ID} obtained by Broberg's theory (60 J/m^2) is much higher than that obtained by the numerical method presented in this study (22 J/m^2). The same trends have been highlighted for porous ceramics and represented in the Fig. 17. In addition, the dynamic fracture energy is also dependent on the porosity rate, and an increase in the porosity rate leads to a decrease in the latter. Given the high velocity of the cracks, the dynamic correction factor obtained by the simulation is always lower than that calculated by the Broberg's theory. The same model as presented before was used in the case of the dynamic fracture energy $G_{IC,num}$ determined by the numerical method to represent these variations with the porosity rate.

This highlights the necessity to take into account inertia effects in the estimate of a fracture parameter with the modified brazilian test applied to alumina sample and to use a rigorous numerical procedure to precisely estimate the dynamic correction factor $g(\dot{a})$ and therefore the dynamic fracture energy G_{ID} (Fig. 18).

5 Effect of porosity rate on local fracture mechanism

SEM observations of the dense (Fig. 18a1, a2), 20micro (Fig. 18b1, b2) and 20meso (Fig. 18c1, c2) show a rough surface near the hole. This roughness is due to micro-damage by initiation of micro-cracks. Given the very heterogeneous microstructure of 60meso (Fig. 18d1, d2), SEM observations at a high magnification do not reveal this damaged zone. This micro-damaged area reveals the size of the crack initiation

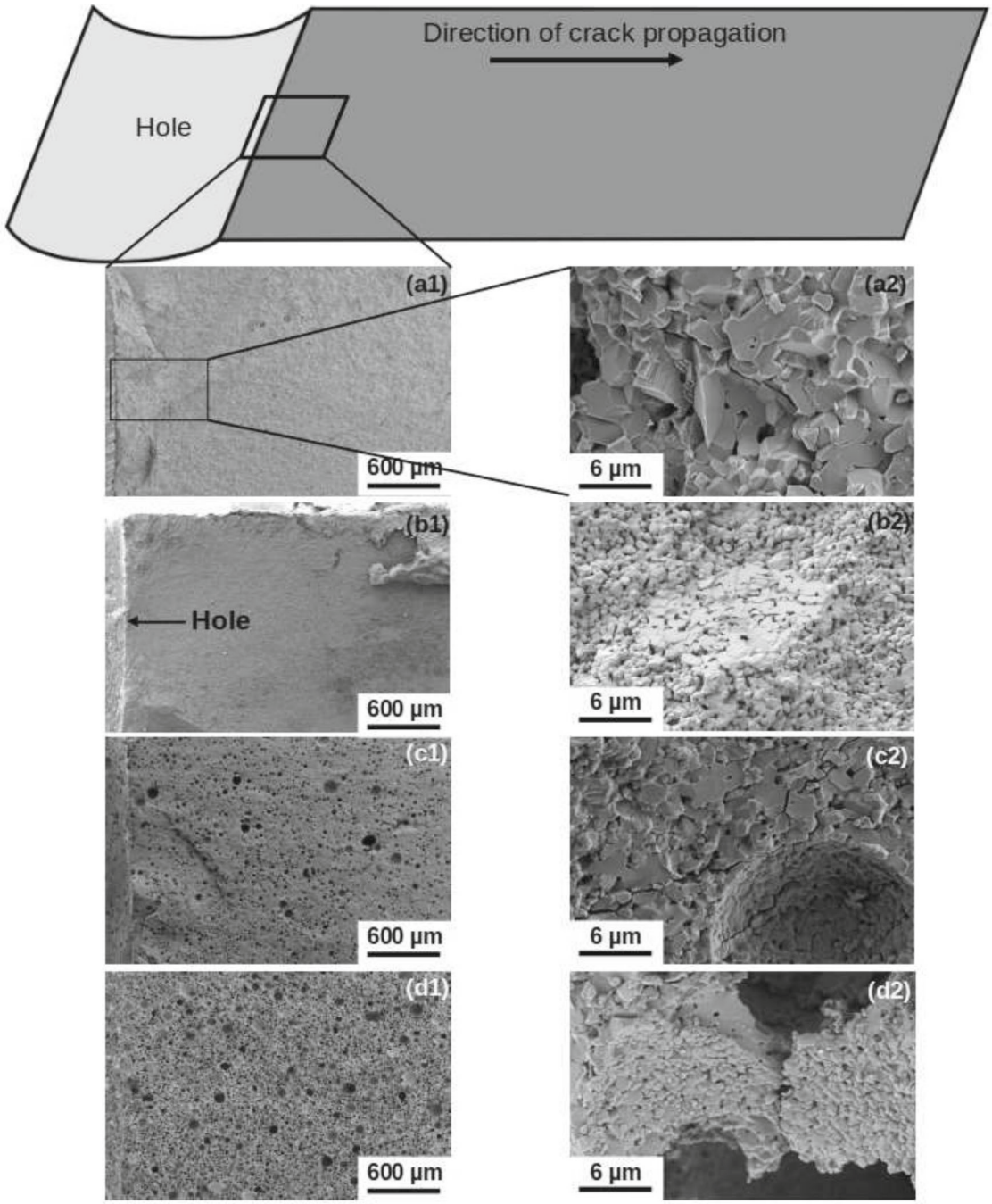

Fig. 18 SEM observations of fracture surface of dynamic modified brazilian sample near the hole: dense (**a1**, **a2**), 20micro (**b1**, **b2**), 20meso (**c1**, **c2**) and 60meso (**d1**, **d2**). The Figures in the second column (X10 000) are a magnification of the Figures in the first column (X100)

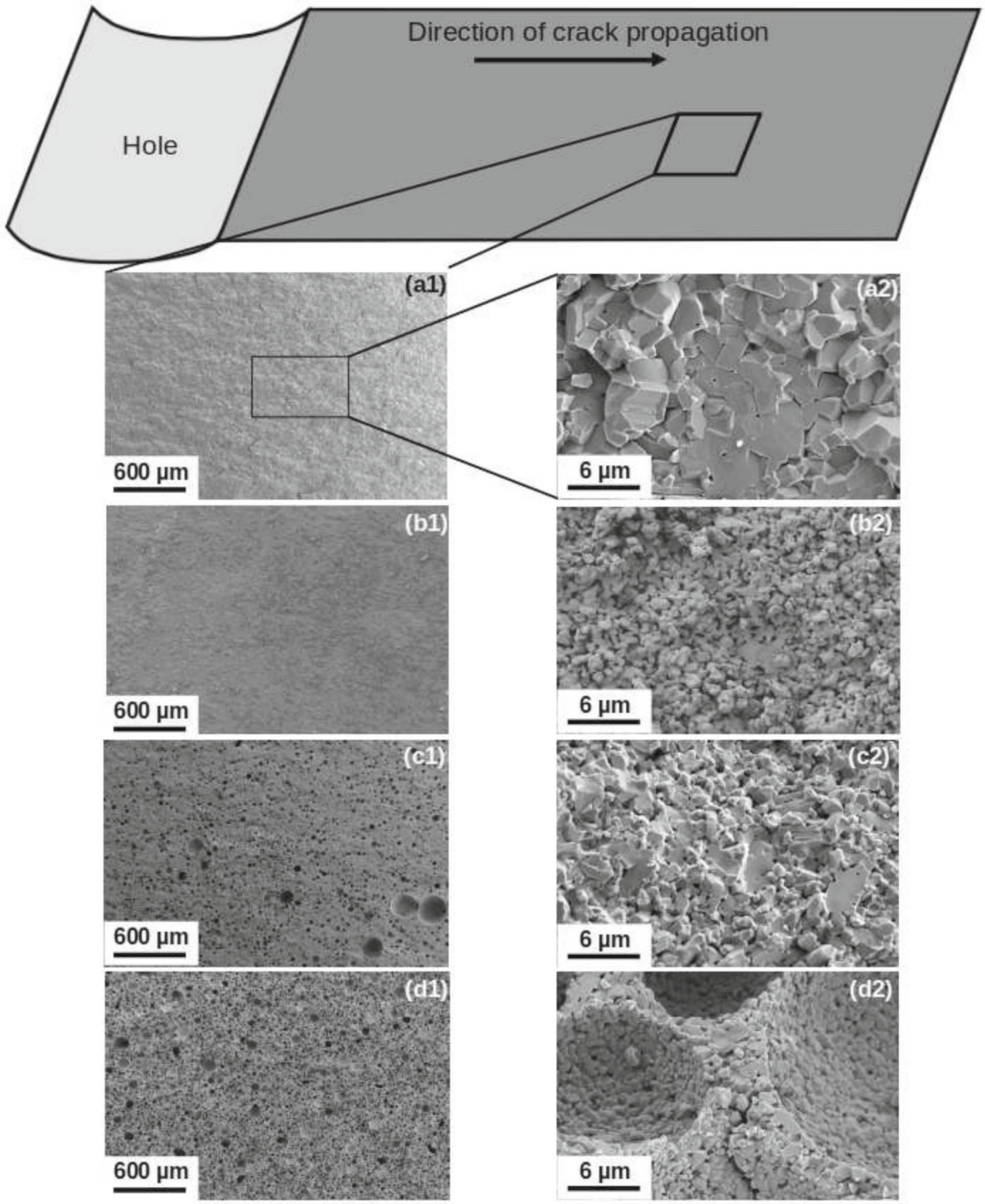

Fig. 19 SEM observations of fracture surface of dynamic modified brazilian sample in the center of the observed face: dense (**a1**, **a2**), 20micro (**b1**, **b2**), 20meso (**c1**, **c2**) and 60meso (**d1**, **d2**). The Figures in the second column (X10 000) are a magnification of the Figures in the first column (X100)

zone. Beyond this damaged zone, the fracture surfaces are smoother, or even flat in the case of dense alumina (Fig. 18a1). At a higher magnification, fracture surface show cleavage zone and large flat grains expected for 20micro interganular patterns are observable. Moreover, Figs. 18a2 and c2 highlight micro-cracks propagating from pore to pore and splitting the grains transgranularly. These SEM observations reveal that the crack propagates in a transgranular way (Fig. 18a2, c2, d2) expect for 20micro where a mixed (trans- and intergranular) mode is observed (Fig. 18b2).

Observation of the fracture surface at a greater distance from the hole shows a rather smooth surface for all grades. At a higher magnification, as previous, a transgranular mode (cleavage zone, flat grains) is observed for dense, 20meso and 60meso grades (Fig. 18a2, c2 and d2). In addition, micro-damage between the pores is observed for the 60meso grade (Figs. 18d2, 19).

6 Conclusions

In order to gain access to relatively small spatial and temporal scales, in situ mode I fracture tests were performed under a synchrotron source. The modified brazilian geometry was used to ensure mode I fracture in the center of the specimen. A Split Pressure Hopkinson bar system was used to dynamically load the specimen. This allowed the *dynamic tensile strength* and fracture energy to be estimated under dynamic loading. *Dynamic tensile strength* decreases with increasing pore volume fraction. The brittle nature of ceramics leads to a *wide scatter* in the results, but this *scatter* decreases with increasing pore volume fraction. Furthermore, at isodensity, the *dynamic tensile strength* seems to depend on the microstructure of the alumina. Indeed, interconnected micropores should be more critical than isolated spherical mesopores.

The geometry used proved to be highly suitable for initiating and isolating a single crack in the dynamic propagation regime, regardless of the ceramic grade studied. For three grades, the maximum theoretical velocity seems to have been reached ($0.6c_R$), and less ($0.4c_R$) for the most porous. Finally, the fracture energy was estimated by numerical simulation. The inertial effects induced by rapid propagation were taken into account. The results obtained highlight the importance of using such a procedure to estimate the fracture energy, otherwise the dynamic effects will be significantly underestimated. To conclude, the dynamic fracture energy G_{ID} is strongly dependent on porosity, decreasing from 22 J/m^2 for a dense material to 5 J/m^2 for alumina with 60% of porosity.

Acknowledgements We acknowledge the European Synchrotron Radiation Facility (ESRF) for providing of synchrotron radiation facilities. We would like to thank the Nouvelle-Aquitaine region and the CEA for funding this research (CERAMOD^2 project) and the company Galtenco solution for the supply of materials. Bratislav Lukć acknowledges the funding from the EPSRC (EP/W003333/1).

Funding Open access funding provided by Arts et Metiers Institute of Technology.

References

Anderson TL (2017) Fracture mechanics: fundamentals and applications. CRC Press, Baco Raton

Arthur Core J-B, Kopp JG, Viot P (2018) Study of the dynamic fracture of hollow spheres under compression using the discrete element method. Procedia Struct Integrity 13:1378–1383

Asadi P, Javad AM, Ali F (2022) Physical and numerical evaluation of effect of specimen size on dynamic tensile strength of rock. Comput Geotech 142:104538

Beguelin PH, Fond C, Kausch HH (1998) The influence of inertial effects on the fracture of rapidly loaded compact tension specimens part a loading and fracture initiation. Int J Fract 89:85–102

Belenky A, Rittel D (2012) Static and dynamic flexural strength of 99.5% alumina. Mech Mater 48:43–55

Belrhiti Y, Dupre JC, Pop O, Germaneau A, Doumalin P, Huger M, Chotard T (2017) Combination of Brazilian test and digital image correlation for mechanical characterization of refractory materials. J Eur Ceram Soc 37(5):2285–2293

Bouras S, Zerizer I, Gheldane F, Bouazza MT, Bouzabata B (2008) Study of the resistance to crack propagation in alumina by acoustic emission. Ceram Int 34(8):1857–1865

Bratislav L, Maria B, Yannick D, Pascal F, Emilio E, Michael R, David C, Daniel E, Margie O, Alexander R (2021) Ultra-

high speed X-ray imaging of dynamic fracturing in cementitious materials under impact. EPJ Web Conf 250:01014
Broberg KB (1960) The propagation of a brittle crack. Arkiv for Fysik
Carneiro FLLB (1943) A new method to determine the tensile strength of concrete. In Proceedings of the 5th meeting of the Brazilian Association for Technical Rules, vol 3, pp. 126–129
Casellas D, Nagl MM, Llanes L, Anglada M (2003) Fracture toughness of alumina and ZTA ceramics: microstructural coarsening effects. J Mater Process Technol 143:148–152
Chapman DJ, Strucka J, Yao Y, Mughal K, Maler D, Efimov S, Belozerov O, Krasik Y, Chittenden JP, Bland SN, Sollier A, Ganzenmuller GC, Cohen A, Levi-Hevroni D, Proud WG, Song P, Eakins DE, Rack A, Lukic B (2024) Dynamic loading platforms coupled to ultra-high speed X-ray imaging at beamline ID19 of the European synchrotron ESRF. High Pressure Res 44:400
Chen Weinong W, Bo S (2010) Split Hopkinson (Kolsky) bar: design, testing and applications. Springer, Berlin
Chen R, Dai F, Qin J, Lu F (2013) Flattened Brazilian disc method for determining the dynamic tensile stress-strain curve of low strength brittle solids. Exp Mech 53:1153–1159
Chen JJ, Guo BQ, Liu HB, Liu H, Chen PW (2014) Dynamic Brazilian test of brittle materials using the split Hopkinson pressure bar and digital image correlation. Strain 50(6):563–570
Croquelois B, Girardot J, Kopp J-B, Cazautets C, Tchoreloff P, Mazel V (2017) Breaking pharmaceutical tablets with a hole: reevaluation of the stress concentration factor and influence of the hole size. Powder Technol 317:126–132
Croquelois B, Kopp JB, Girardot J, Tchoreloff P, Mazel V (2021) Dynamic fracture analysis in Brazilian test: application to pharmaceutical tablets. Int J Fract 229(1):113–124
De Aza AH, Chevalier J, Fantozzi G, Schehl M, Torrecillas R (2002) Crack growth resistance of alumina, zirconia and zirconia toughened alumina ceramics for joint prostheses. Biomaterials 23(3):937–945
Deng Z-Y, Fukasawa T, Ando M, Zhang G-J, Ohji T (2001) Microstructure and mechanical properties of porous alumina ceramics fabricated by the decomposition of aluminum hydroxide. J Am Ceram Soc 84(11):2638–2644
Denoual C, Hild F (2000) A damage model for the dynamic fragmentation of brittle solids. Comput Methods Appl Mech Eng 183(3–4):247–258
Doitrand A, Molnár G, Leguillon D, Martin E, Carrère N (2022) Dynamic crack initiation assessment with the coupled criterion. Eur J Mech-A/Solids 93:104483
Duplan Y (2020) Caractérisation expérimentale et modélisation des propriétés de rupture et de fragmentation dynamiques d'un noyau de munition et de céramiques à blindage. PhD thesis, Université Grenoble Alpes [2020-....]
Fairhurst C (1964) On the validity of the 'Brazilian' test for brittle materials. In International journal of rock mechanics and mining sciences & geomechanics abstracts, vol 1, pp 535–546. Elsevier
Freund LB (1998) Dynamic fracture mechanics. Cambridge University Press, Cambridge
García VJ, Márquez CO, Zúñiga-Suárez AR, Zuñiga-Torres BC, Villalta-Granda LJ (2017) Brazilian test of concrete specimens subjected to different loading geometries. Int J Concrete Struct Mater 11:343–363
Gaüzère L, Besnard C, Pontoreau M, Carlotti S, Couillaud S, Heintz J-M (2023) Influence of the acrylamide-based monomer on the sintering of ceramics shaped by gelcasting. Open Ceram 16:100447
Griffith Alan Arnold (1921) IV. The phenomena of rupture and flow in solids. Philos Trans Royal Soc London Ser A 221(582–593):163–198
Hans J, Schneider Gerold A (2019) Fracture toughness of porous materials-experimental methods and data. Data Brief 23:103709
Herbert K (1949) An investigation of the mechanical properties of materials at very high rates of loading. Proc Phys Soc Sect B 62(11):676
Hiestand EN, Wells JE, Peot CB, Ochs JF (1977) Physical processes of tableting. J Pharm Sci 66(4):510–519
Hobbs DW (1965) An assessment of a technique for determining the tensile strength of rock. Br J Appl Phys 16(2):259
Hong C, Zhang X, Han J, Wang B (2006) Fabrication and mechanical properties of porous TIB 2 ceramic. J Mater Sci 41:4790–4794
Jelitto H, Schneider GA (2020) Extended cubic fracture model for porous materials and the dependence of the fracture toughness on the pore size. Materialia 12:100761
Ji M, Li H, Zheng J, Yang S, Zaiemyekeh Z, Hogan JD (2022) An experimental study on the strain-rate-dependent compressive and tensile response of an alumina ceramic. Ceram Int 48(19):28121–28134
Kopp J-B (2013) Etude de la rupture dynamique de tuyaux polymères utilisés pour le transport du gaz sous moyenne pression. PhD thesis, Strasbourg
Kopp J-B, Schmittbuhl J, Noel O, Lin J, Fond C (2014) Fluctuations of the dynamic fracture energy values related to the amount of created fracture surface. Eng Fract Mech 126:178–189
Kopp J-B, Lin J, Schmittbuhl J, Fond C (2014) Longitudinal dynamic fracture of polymer pipes. Eur J Environ Civ Eng 18(10):1097–1105
Li X, Qiuhong W, Tao M, Weng L, Dong L, Zou Y (2016) Dynamic Brazilian splitting test of ring-shaped specimens with different hole diameters. Rock Mech Rock Eng 49:4143–4151
Longchamps V (2024) Modélisation du comportement de céramiques projetées plasma sous choc par simulation discrète à l'échelle de la microstructure. PhD thesis, HESAM université
Mazel V, Guerard S, Croquelois B, Kopp J-B, Girardot J, Diarra H, Busignies V, Tchoreloff P (2016) Reevaluation of the diametral compression test for tablets using the flattened disc geometry. Int J Pharm 513(1–2):669–677
Nilsson F (1972) Dynamic stress-intensity factors for finite strip problems. Int J Fract Mech 8:403–411
Nishioka T (1997) Computational dynamic fracture mechanics. Int J Fract 86:127–159
Olbinado MP, Just X, Gelet J-L, Lhuissier P, Scheel M, Vagovic P, Sato T, Graceffa R, Schulz J, Mancuso A et al (2017) MHZ frame rate hard X-ray phase-contrast imaging using synchrotron radiation. Opt Express 25(12):13857–13871

Paliwal B, Ramesh KT (2008) An interacting micro-crack damage model for failure of brittle materials under compression. J Mech Phys Solids 56(3):896–923

Popelar CH, Atkinson C (1980) Dynamic crack propagation in a viscoelastic strip. J Mech Phys Solids 28(2):79–93

Quentin H, Philippe V, Louise LB, Antonio C, Kopp J-B (2024) Influence of the microstructure on the compressive behaviour of porous aluminas: from microstructural characterisation to fracture mechanisms. J Eur Ceram Soc 44:4170

Ravi-Chandar K, Knauss WG (1984) An experimental investigation into dynamic fracture: Iii. On steady-state crack propagation and crack branching. Int J Fract 26:141–154

Robinson P, Song DQ (1992) A modified DCB specimen for mode I testing of multidirectional laminates. J Compos Mater 26(11):1554–1577

Rubio Ruiz RA, Pournoori N, Isakov M, Saksala T, Bjørge R, Rack A, Lukic B, Cohen A, Levi-Hevroni D, Kane PA, Hokka M (2024) Progressive weakening of granite by piezoelectric excitation of quartz with alternating current. Rock Mech Rock Eng. https://doi.org/10.1007/s00603-024-03948-w

Sawaki Y, Nagase Y, Yoshida H, Inoue A, Fujiwara T (1993) Crack propagation behavior in alumina ceramic under static and cyclic loading. JSME Int J Ser A Mech Mater Eng 36(4):354–360

Scapin M, Peroni L, Avalle M (2017) Dynamic Brazilian test for mechanical characterization of ceramic ballistic protection. Shock Vib 2017:7485856

Singh D, Shetty DK (1989) Fracture toughness of polycrystalline ceramics in combined mode I and mode II loading. J Am Ceram Soc 72(1):78–84

Thiercelin M, Roegiers J-C (1988) Fracture toughness determination with the modified ring test. In Proceedings of the international symposium on engineering in complex rock formations, pp 284–290. Elsevier,

Tomaszewski H, Boniecki M, Weglarz H (2000) Effect of grain size on r-curve behaviour of alumina ceramics. J Eur Ceram Soc 20(14–15):2569–2574

Tutluoglu L, Keles C (2012) Effects of geometric factors on mode I fracture toughness for modified ring tests. Int J Rock Mech Min Sci 51:149–161

Vekinis G, Ashby MF, Beaumont PWR (1990) R-curve behaviour of Al_2O_3 ceramics. Acta Metall Mater 38(6):1151–1162

Wang QZ, Jia XM, Kou SQ, Zhang ZX, Lindqvist P-A (2004) The flattened Brazilian disc specimen used for testing elastic modulus, tensile strength and fracture toughness of brittle rocks: analytical and numerical results. Int J Rock Mech Min Sci 41(2):245–253

Wilson E, Bathe K-J (1976) Numerical methods in finite element analysis. Prentice-Hall, Hoboken

Yoffe EH (1951) The moving griffith crack. London Edinburgh Dublin Philos Mag J Sci 42(330):739–750

Zheng J, Li H, Hogan JD (2023) Strain-rate-dependent tensile response of an alumina ceramic: experiments and modeling. Int J Impact Eng 173:104487

Terms and Conditions

Springer Nature journal content, brought to you courtesy of Springer Nature Customer Service Center GmbH (“Springer Nature”).
Springer Nature supports a reasonable amount of sharing of research papers by authors, subscribers and authorised users (“Users”), for small-scale personal, non-commercial use provided that all copyright, trade and service marks and other proprietary notices are maintained. By accessing, sharing, receiving or otherwise using the Springer Nature journal content you agree to these terms of use (“Terms”). For these purposes, Springer Nature considers academic use (by researchers and students) to be non-commercial.
These Terms are supplementary and will apply in addition to any applicable website terms and conditions, a relevant site licence or a personal subscription. These Terms will prevail over any conflict or ambiguity with regards to the relevant terms, a site licence or a personal subscription (to the extent of the conflict or ambiguity only). For Creative Commons-licensed articles, the terms of the Creative Commons license used will apply.
We collect and use personal data to provide access to the Springer Nature journal content. We may also use these personal data internally within ResearchGate and Springer Nature and as agreed share it, in an anonymised way, for purposes of tracking, analysis and reporting. We will not otherwise disclose your personal data outside the ResearchGate or the Springer Nature group of companies unless we have your permission as detailed in the Privacy Policy.
While Users may use the Springer Nature journal content for small scale, personal non-commercial use, it is important to note that Users may not:

1. use such content for the purpose of providing other users with access on a regular or large scale basis or as a means to circumvent access control;
2. use such content where to do so would be considered a criminal or statutory offence in any jurisdiction, or gives rise to civil liability, or is otherwise unlawful;
3. falsely or misleadingly imply or suggest endorsement, approval , sponsorship, or association unless explicitly agreed to by Springer Nature in writing;
4. use bots or other automated methods to access the content or redirect messages
5. override any security feature or exclusionary protocol; or
6. share the content in order to create substitute for Springer Nature products or services or a systematic database of Springer Nature journal content.

In line with the restriction against commercial use, Springer Nature does not permit the creation of a product or service that creates revenue, royalties, rent or income from our content or its inclusion as part of a paid for service or for other commercial gain. Springer Nature journal content cannot be used for inter-library loans and librarians may not upload Springer Nature journal content on a large scale into their, or any other, institutional repository.
These terms of use are reviewed regularly and may be amended at any time. Springer Nature is not obligated to publish any information or content on this website and may remove it or features or functionality at our sole discretion, at any time with or without notice. Springer Nature may revoke this licence to you at any time and remove access to any copies of the Springer Nature journal content which have been saved.
To the fullest extent permitted by law, Springer Nature makes no warranties, representations or guarantees to Users, either express or implied with respect to the Springer nature journal content and all parties disclaim and waive any implied warranties or warranties imposed by law, including merchantability or fitness for any particular purpose.
Please note that these rights do not automatically extend to content, data or other material published by Springer Nature that may be licensed from third parties.
If you would like to use or distribute our Springer Nature journal content to a wider audience or on a regular basis or in any other manner not expressly permitted by these Terms, please contact Springer Nature at

onlineservice@springernature.com